Journal of Power Sources 195 (2010) 7316–7322

Contents lists available at ScienceDirect

Journal of Power Sources

journal homepage: www.elsevier.com/locate/jpowsour

In situ quantification of the in-plane water content in the Nafion® membrane of an operating polymer-electrolyte membrane fuel cell using ^{1}H micro-magnetic resonance imaging experiments

Mingtao Wang, Kirk W. Feindel, Steven H. Bergens*, Roderick E. Wasylishen**

Department of Chemistry, University of Alberta, E3-24 Gunning/Lemieux Chemistry Center, Edmonton, Alberta, Canada T6G 2G2

ARTICLE INFO

Article history:
Received 31 March 2010
Received in revised form 14 May 2010
Accepted 17 May 2010
Available online 20 June 2010

Keywords:
Water content
Nafion® membrane
PEMFC
^{1}H micro-MRI
Calibration curve

ABSTRACT

Spatial, quantitative, and temporal information regarding the water content distribution in the transverse-plane between the catalyst layers of an operating polymer-electrolyte membrane fuel cell (PEMFC) is essential to develop a fundamental understanding of water dynamics in these systems. We report ^{1}H micro-magnetic resonance imaging (MRI) experiments that measure the number of water molecules per SO_3H group, λ, within a Nafion®-117 membrane between the catalyst stamps of a membrane-electrode assembly, MEA. The measurements were made both *ex situ*, and inside a PEMFC operating on hydrogen and oxygen. The observed ^{1}H MRI T_2 relaxation time of water in the PEM was measured for several known values of λ. The signal intensity of the images was then corrected for T_2 weighting to yield proton density-weighted images, thereby establishing a calibration curve that correlates the ^{1}H MRI density-weighted signal with λ. Subsequently, the calibration curve was used with proton density weighted (i.e., T_2-corrected) signal intensities of transverse-plane ^{1}H MRI images of water in the PEM between the catalyst stamps of an operating PEMFC to determine λ under various operational conditions. For example, the steady state, transverse-plane λ was 9 ± 1 for a PEMFC operating at ~26.4 mW cm^{-2} (~20.0 mA, ~0.661 V, 20 °C, flow rates of the dry H_2(g) and O_2(g) were 5.0 and 2.5 mL min^{-1}, respectively).

1. Introduction

Polymer-electrolyte membrane fuel cells, PEMFCs, are being considered for transportation and related applications due to their high-power density and relative simplicity [1–3]. The amount of water in the gas flow fields, the gas-diffusion and catalyst layers, and in the polymer-electrolyte membrane, PEM, strongly determines the performance of a PEMFC [4–7]. For example, excess water in the gas flow channels or in the gas-diffusion and catalyst layers will block the transport of reactant gases, thereby reducing the efficiency of the cell, and accelerating catalyst layer degradation. Low levels of water in the PEM decrease proton conductivity and accelerate degradation. The distribution of water among the components of an operating PEMFC is dynamic, and depends upon parameters such as cell voltage, current, temperature, gas humidification, gas flow rates, load variation, and PEM pretreatment [8–12].

The PEM in a PEMFC acts as the proton conductor, electron insulator, reactant gas barrier, and support of the catalyst layers [1–3]. Resistance to proton conduction, or ionic resistance, through a PEM is strongly influenced by its water content [12–14]. Nafion® is the most common type of PEM used in PEMFCs, and the behavior, nature, transport, and uptake of water in Nafion® has been extensively studied [10–12]. The specific proton conductivity of Nafion®-117 was shown to increase linearly with the number of water molecules absorbed per SO_3H group, λ, after equilibration with different water vapor pressures at 30 °C [10]. The maximum amount of water adsorbed per SO_3H group, $\lambda_{max} \sim 22$, is obtained when the so-called expanded, or E-form of Nafion®-117 is immersed in liquid water at 27 °C [10,12]. In contrast, $\lambda_{max} \approx 14$ when expanded Nafion®-117 is exposed to saturated water vapor at 27 °C [10,12]. Expanded Nafion® can be prepared by immersion in boiling water followed by drying under vacuum at room temperature. Drying under harsher conditions forms the so-called normal and shrunken forms of Nafion® which have lower values of λ_{max} [11].

Spatial, quantitative, and temporal information regarding λ in the region of PEMs between the catalyst layers of operating PEMFCs, that is, within the membrane-electrode assembly, MEA, is necessary to develop a fundamental understanding of water dynamics in these systems. Such a fundamental understanding

* Corresponding author. Tel.: +1 780 492 9703; fax: +1 780 492 8231.
** Corresponding author. Tel.: +1 780 492 4336; fax: +1 780 492 8231.
E-mail addresses: steve.bergens@ualberta.ca (S.H. Bergens), Roderick.wasylishen@ualberta.ca (R.E. Wasylishen).

0378-7753/$ – see front matter © 2010 Elsevier B.V. All rights reserved.
doi:10.1016/j.jpowsour.2010.05.029

will aid the development of improved membranes, the modeling of water dynamics in PEMs under load, and the optimization of PEMFC performance, lifetime, and design [1–3,13,14]. Various experimental techniques are being developed to investigate water in different components of operating PEMFCs. These methods have recently been reviewed [15,16]. The methods that investigate water in PEMs between the catalysts layers of MEAs include ionic conductivity measurements [17–25], neutron imaging [26–34,21], X-ray diffraction studies [35–37], micro-Raman measurements [38], fluorescence spectroscopy [39], interferometric tomography [40], ^{1}H magnetic resonance imaging (MRI) [41–51], and infrared spectroscopy [52].

A major advantage of MRI is that it allows one to observe the *in situ* water distribution in the transverse-plane (also referred to as the in-plane distribution) of the membrane within the MEA between the catalysts of an operating PEMFC [48–50]. In other words, one is observing the in-plane water density, as opposed to looking at the membrane edge-on. Such observations are critical because the transverse-plane distribution of water within the PEM between the catalyst layers of an operating PEMFC is often not homogeneous. This distribution depends upon factors including the relative flow directions and rates of the anode and cathode gas streams, catalyst stamp edge effects, membrane deformations (e.g., swelling, bending or buckling), the presence of liquid water drops in contact with regions of the membrane, grooves in the gas flow channels, and inhomogeneities in the gas-diffusion layers and catalyst stamps. In fact, it seems unlikely that a homogeneous in-plane distribution of water exists in the PEMs of operating fuel cells with liquid water present in the GDL or gas flow channels. One-dimensional, edge-on observations of water in PEM's are not currently suited to observe transverse-plane inhomogeneities in water distribution. Several groups have reported *in situ* localized PEM ionic resistance studies that were carried out with electrode arrays [21–24]. Three types of direct observations of transverse-plane distributions of water in the PEM of a fuel cell have been reported. A 2006 report describes neutron scattering experiments to observe water in the transverse-plane of a Gore^{TM} 5510 PEM within the MEA of a PEMFC [53]. These observations were made after the PEMFC was stopped, and the liquid water was flushed from the flow fields and gas-diffusion layers. A recent, preliminary report describes interferometric tomographic observations of changes in water content in a Nafion® membrane within a non-operating fuel cell [40]. There are several reports of *in situ* observations of the transverse-plane PEM distribution of water within the MEA of PEMFCs under a variety of operating conditions and varying loads using MRI [48–50,54]. Most of these MRI investigations are qualitative (e.g., Refs. [48–50]). Tsushima et al. [54] investigated the in-plane water distribution using MRI; these authors provided quantitative results although details of how such information was obtained were not offered.

To our knowledge, ^{1}H MRI is the only reported spectroscopic technique to make *in situ* observations of transverse plane H_2O in the PEM between the catalysts of an operating fuel cell. To obtain the in-plane water content in the PEM of an operating PEMFC, a calibration curve that relates signal intensity of ^{1}H MRI images to λ is necessary. Dunbar and Masel [41,55] quantified the ^{1}H MRI signal for water using water-filled capillaries placed in the cell housing as the calibration standards. Tsushima and coworkers [56–59] used a calibration curve obtained from ^{1}H MRI images of an MEA exposed to reactant gases with known relative humidity to quantify the through-plane absolute water content distribution. One drawback of these calibration methods is the neglect of nuclear spin relaxation effects on the signal intensity of the ^{1}H MRI images. As noted by Zhang et al. [51], the signal intensity of the ^{1}H MRI images for water in the PEM of operating PEMFCs is influenced by the local ^{1}H T_2 relaxation times. Inherent in MRI experiments is a delay between NMR signal excitation and signal acquisition (i.e., the so-called echo time) which results in an attenuation of the signal intensity of MRI images. Single point imaging methods [60,61] based on pure phase-encoding and ultra-short echo time MRI pulse sequences [62,63] are examples of MRI techniques that allow experimentalists to use short (e.g., 1 ms) or ultra-short (e.g., 100 μs) echo times to minimize the effects of T_2 weighting. However, if the protons present have a short T_2 value relative to the echo time, the effect of T_2 relaxation on the signal intensity must be taken into account if quantitative results are desired. Corrections for ^{1}H T_2 relaxation are critical in any discussion of water quantification using MRI.

In this work, ^{1}H micro-MRI experiments were used to determine λ in the Nafion® membrane of an operating PEMFC. A calibration curve that relates λ with ^{1}H density-weighted signal intensity of the corresponding ^{1}H MRI image was first established on a PEM with catalyst stamps outside of the PEMFC. Subsequently, this calibration curve is used to determine *in situ* λ values in an operational PEMFC.

2. Magnetic resonance imaging (MRI) background

Magnetic resonance imaging, MRI, is a powerful non-invasive visualization technique that is widely used in medicine [64]; however, the technique is also finding a wide range of applications in materials science [65–68]. Most MRI experiments are designed to provide two-dimensional profiles or "pictures" of ^{1}H (proton) density in an object. Because water is the most abundant source of protons in the human body, it is water that is detected in most MRI experiments. Applications of MRI to specifically monitor water in operating fuel cells have recently been reviewed by Feindel et al. [49] and by Tsushima and Hirai [59]. Although the fundamental principles and important parameters necessary to perform MRI experiments are outlined in the latter two reviews and numerous textbooks, it is important to remind readers of some of theses parameters.

When an object containing protons (e.g., water) is placed in the strong applied magnetic field, B_0, necessary for conducting an MRI experiment, it takes a finite time for the bulk magnetization of the object to approach thermal equilibrium. The first-order time constant that describes the process by which the magnetization of the proton nuclei (i.e., ^{1}H) approach thermal equilibrium along the direction of the applied magnetic field is the spin–lattice relaxation time, T_1. This magnetization along the direction of the applied magnetic field is referred to as the longitudinal magnetization. In time $3T_1$, the longitudinal magnetization will be approximately 95% of the equilibrium value while after time $5T_1$, this value will be 99.3%. In practice, spin-lattice relaxation times are measured using the inversion-recovery pulse sequence [65–67]. For pure liquid water at 293 K, the $T_1(^1\text{H})$ is approximately 3 s; if the rotational motion of water is partially restricted, the $T_1(^1\text{H})$ values tend to decrease. In MRI experiments it is desirable to manipulate the equilibrium or near equilibrium magnetization, thus the time constant, T_1 is important (vide infra).

The spin–spin relaxation time, T_2, describes the first-order time constant that governs the bulk magnetization vector in the plane perpendicular to the applied magnetic field (the so-called transverse magnetization in the *xy*-plane). For pure water, T_2 is approximately 2 s, and this value decreases as water mobility is impeded [69]. Experimentally, T_2 values are measured with the basic spin-echo (SE) pulse sequence originally described by Hahn [70], or with some minor variation thereof [71,72]. The SE experiment forms the basis of the imaging pulse sequence used in the present investigation.

The MRI experiment involves applying a series of RF pulses that perturb the "equilibrium" longitudinal magnetization, M_z. In order to obtain reasonably quantitative measurements of proton (water)

Table 1
^{1}H $T_{2,obs}$ values for the PEM at various λ values.

λ	$T_{2,obs}$ (ms)
11.5 ± 0.5	40 ± 2
10.5 ± 0.5	35 ± 3
9.5 ± 0.5	30 ± 4
8.9 ± 0.5	29 ± 3
8.3 ± 0.5	28 ± 3
7.3 ± 0.5	25 ± 4
6.0 ± 0.5	20 ± 3

density, it is important that the time between perturbing RF pulses, *TR*, be greater than $3T_1$. Also, inherent in any MRI experiment is the finite time between RF excitation and signal acquisition, *TE*. Since, one detects the net magnetization in the *xy*-plane, it is important that *TE* be as short as possible, certainly much less than T_2. The "observed" or measured transverse magnetization is given by:

$$M_{xy}(\text{obs.}) = M_{xy}(t = 0)\exp(-TE/T_2) \quad (1)$$

For a complex system such as water distributed in a Nafion® membrane of an operating fuel cell, there will undoubtedly be a distribution of T_2 values. In membrane regions of high water content, the ^{1}H T_2 values are expected to be long, whereas in regions of low water content the T_2 values may be short [73]. Clearly, the ^{1}H T_1 and T_2 values will be greater the larger the value of λ—the number of water molecules per SO_3H group. Finally, it is well known that the conductivity of Nafion® increases with water content [10–12].

Further details concerning MRI parameters can be found in our review and references there-in. Also, the review of Mauritz and Moore [14] is an important source of information about the state of water in Nafion®.

3. Experimental

3.1. Ex situ determination of λ in the Nafion®-117 membrane

The Nafion®-117 membrane with an equivalent weight of 1100 g equiv^{-1} and a thickness of 7 mil (i.e., 178 μm) was used to fabricate the MEA. The MEA was assembled by hot-pressing at 120 °C [74] with unsupported HiSpec 1000 Pt black and HiSpec 6000 Pt–Ru black for the cathode and anode catalyst (loadings ~2–3 mg cm^{-2}), respectively. The geometric area of the catalyst decals is ~0.5 cm^2. A roughly square PEM (~0.8 cm sides) containing the MEA was used in the experiments to determine the λ values. The sides of the PEM were slightly larger than the diameter of the MEA. The MEA and surrounding PEM were dried and heat-pressed at 120 °C in the preparation of the MEA. The MEA was saturated by immersion in distilled water at room temperature for ~1 h for the maximal uptake of water. It was then blotted dry to remove the excess surface water and quickly put into a sealed glass container. In each case the MEA was weighed in the container, and the sealed container was then immediately inserted into the MRI resonator. PEMs with λ values between zero and saturation were prepared by partial dehydration of the saturated PEM. Each experiment was repeated five times to ensure consistent results. Complete dehydration of the PEM was achieved by first drying it at room temperature for 24 h and then at 105 °C for 1 h in a vacuum oven [12]. The mass-difference between the wet and dry PEM and the equivalent weight, EW, of Nafion®-117 were used to determine the λ values (Table 1). The EW in g equiv^{-1} of a polymer membrane can be expressed:

$$\text{EW} = 100n + 446 \quad (2)$$

where *n* is the number of tetrafluorethylene groups on average per perfluoro-sulfonylfluoride ethyl-propyl-vinyl ether (PSEPVE) monomer. With known *n* values, the molar mass of the PSEPVE monomer can be calculated. This information, together with the mass of the dried PEM and the mass of water, was used to determine the λ values.

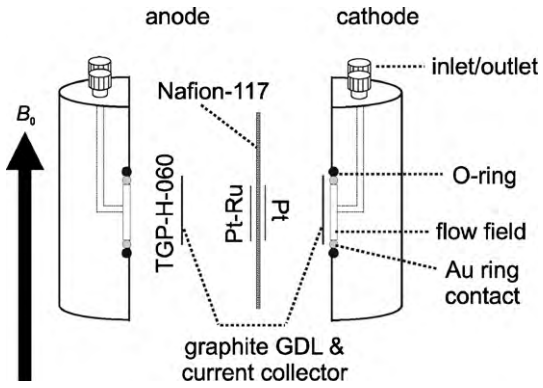

Fig. 1. Schematic of the PEMFC assembly indicating the location of various components and the orientation of the cell with respect to the external applied magnetic field, B_0.

3.2. Operating PEMFC

The design and experimental set-up of the PEMFC used in our lab are described elsewhere [49,50]. As shown in Fig. 1, the MEA is sandwiched between Toray TGP-H-060 gas-diffusion layers (GDLs) with its plane parallel to the applied magnetic field, B_0. Reactant gas flow channels are compressed against the GDLs, with adjustable co/counter-flow configurations. Before operation, the PEM was humidified by filling the anode gas flow field with water. After humidification, the cell was operated on pre-purified H_2(g) (99.995%) and industrial-grade O_2(g) (99.0%), supplied at ambient pressure to the PEMFC from compressed gas cylinders *via* flow meters. Unless otherwise stated, the flow rates of the dry H_2(g) and O_2(g) were set to 5.0 and 2.5 mL min^{-1}, respectively. The electrical load was controlled using a variable resistor, and the voltage and current were monitored using Radio Shack 22-805 multi-meters. The cell was operated at 20 °C.

3.3. Proton MRI experiments

Proton micro-MRI experiments were performed using a 7.05 T (300.17 MHz for ^{1}H) wide-bore (89 mm) superconducting magnet, a Bruker Avance 300 console, a Micro-2.5 imaging accessory, and a 30 mm birdcage resonator. The water-cooled gradient unit was maintained at 20 °C for all the imaging experiments. For *ex situ* determination of λ as described in Section 3.1, the capped glass container containing the PEM was inserted into the resonator and its location was carefully adjusted so that the PEM was positioned approximately at the iso-center of the resonator with its plane perpendicular to B_0. For imaging experiments on the operating PEMFC, the cell assembly was carefully positioned and orientated within the birdcage resonator and the gradient set to yield the best sensitivity. In all imaging experiments, a multi-slice multi-echo spin-echo imaging pulse sequence (MSME) was used to acquire images from a 30 mm × 30 mm field of view. Each image was obtained in a single MSME experiment with eight echoes acquired after each excitation. 128 frequency and phase-encoding steps were used, yielding an in-plane pixel size of 0.234 mm × 0.234 mm. The slice thickness was 0.5 mm. The time between ^{1}H NMR signal excitation and acquisition of the first echo, *TE*, was 3.2 ms. The repetition time between successive ^{1}H NMR signal excitations, *TR*, was 1.0 s, resulting in a total time of 128 s per image acquisition. The receiver bandwidth was approximately 101 kHz.

4. Results and discussion

4.1. The calibration curve

The λ values, determined by mass-difference, for different hydration levels of the PEM are shown in Table 1. The maximal rehydration of the PEM at ambient temperature resulted in a λ value of 11.5 ± 0.5. Nafion®-117 is known to have λ values in the range of ~2–22; however, if the membrane is dried at a temperature greater than 105 °C, the maximum λ value at a rehydration temperature lower than 30 °C is approximately 12 [10,12]. The MEA used here for establishing the calibration curve was prepared by hot-pressing the catalyst stamps into the membrane at 120 °C, and the resultant maximal water uptake reported herein agrees well with that reported in the literature [12]. Note that there is PEM beyond the MEA catalyst decals; λ is anticipated to be the same for the PEM contained in the MEA and the PEM beyond the decal since they were both hot-pressed in the preparation of the MEA. Indeed, as shown in Fig. 2(a), the difference in T_2-weighted ^{1}H MRI intensity between the two areas is less than 10%.

The signal intensity of the ^{1}H MRI images of the PEM at various λ values was determined from the region of interest (ROI) (Fig. 2(a)), which is restricted to the MEA area and contains the PEM between the catalyst layers. This area of the PEM was selected because it has the greatest influence on cell performance. In the analyses of the ^{1}H MRI images of the operating PEMFC, the ROI used was the same as that used in our previous work [49,50,75,76]. Note that the ^{1}H NMR signal for H_2O in the GDLs and catalyst layers is not observed due to magnetic susceptibility variation induced frequency shifts, in addition to rapid NMR relaxation processes. As a result, signal intensity in this ROI represents water in the PEM between the attached catalyst layers.

The signal intensity of a ^{1}H MRI image is influenced by factors such as the local proton density and relaxation time constants (e.g., ^{1}H T_1 and T_2). To ensure that the intensity accurately represents the local proton density, weighting factors other than that from the proton density must be removed. T_1-weighting can be eliminated using a *TR* greater than $5T_1$. NMR studies of Nafion® membranes showed that water molecules in these membranes are characterized by mono-exponential ^{1}H T_1 and T_2 values, and that the ^{1}H T_1 values are typically less than 200 ms [77,78]. In the case of operating PEMFCs, the presence of paramagnetic components in the MEA (e.g., catalysts, O_2(g)) may further reduce the ^{1}H T_1 values. Consequently, a *TR* value of 1.0 s is sufficient to remove T_1-weighting and was used for the imaging experiments reported herein (^{1}H MRI experiments using a *TR* of 5.0 s for the PEM with maximum water content yielded the same result). Dephasing of the transverse magnetization, resulting in a decay of the NMR signal, can be caused by many factors. For example, B_0 field inhomogeneity and local magnetic susceptibility variations enhance dephasing of the transverse magnetization, in addition to homogeneous, irreversible T_2 relaxation. Also, diffusion of water molecules within the PEM attenuates the transverse magnetization due to the random movement of water molecules through local magnetic field variations. In the case of operating PEMFCs, proton conduction from the anode to the cathode and the associated water-transport processes may also affect the transverse magnetization. Some dephasing of the transverse magnetization, such as that caused by B_0 field inhomogeneity, can be reversed using a SE MRI experiment. To a good approximation, the inter-play of all these attenuation mechanisms results in a single observable (apparent) ^{1}H T_2 value for water molecules in the PEM; this value is different from the intrinsic ^{1}H T_2 value and will hereafter be denoted ^{1}H $T_{2,obs}$. The observed ^{1}H T_2 value, $T_{2,obs}(x, y)$, obtained from a SE experiment, was assumed to account for the various transverse magnetization attenuation mechanisms. For a ^{1}H MRI image obtained using a SE pulse sequences with $TR \geq 5T_1$,

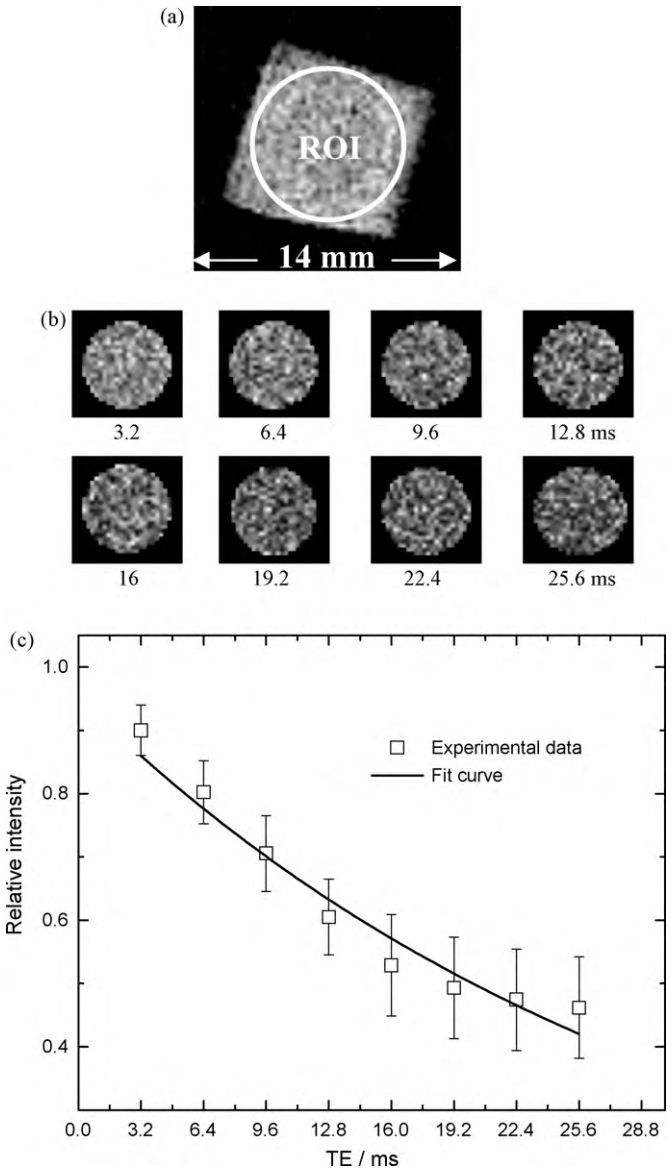

Fig. 2. (a) ^{1}H MRI image of the PEM with λ = 8.9 ± 0.5 showing the region of interest, ROI, which corresponds to the area of the catalyst decal. (b) ^{1}H MRI images of the ROI from the PEM at eight different echo times (i.e., *TE* values). (c) Intensity of the ^{1}H MRI images of the ROI vs. *TE*. The relaxation decay curve was fitted with a single-component exponential decay function. Image acquisition parameters: (a) SE, *TR* = 1.0 s, *TE* = 3.2 ms, FOV = 30 mm × 30 mm, pixel size = 234 μm × 234 μm, slice thickness = 0.5 mm, eight echoes per image, one average. (b) Same as (a) except one image for each echo with varying values of *TE*.

the intensity of the signal for a pixel can be expressed as:

$$S(x, y) \propto \rho_0(x, y) \exp(-nTE/T_{2,obs}(x, y)) \quad (3)$$

where $S(x, y)$ is the signal intensity of the pixel, $\rho(x, y)$ is the local proton density, and n is the echo number.

^{1}H $T_{2,obs}$ values for the PEM at various λ values were measured using a multiple-echo SE pulse sequence [65]. Using this pulse sequence, eight echo images were acquired and the signal intensity of the images were modulated by $\exp(-nTE/T_{2,obs})$, where n ranges from 1 to 8, and $TE = 3.2$ ms (see Fig. 2(b) where λ = 8.9 ± 0.5). The decay of the transverse magnetization was fitted by a single exponential decay function (Fig. 2(c)). The determined ^{1}H $T_{2,obs}$ values are shown in Table 1; the data indicate that the value of ^{1}H $T_{2,obs}$ increases with the hydration level of the PEM, which is consistent with findings by Zhang et al. [51]. Nafion® membranes

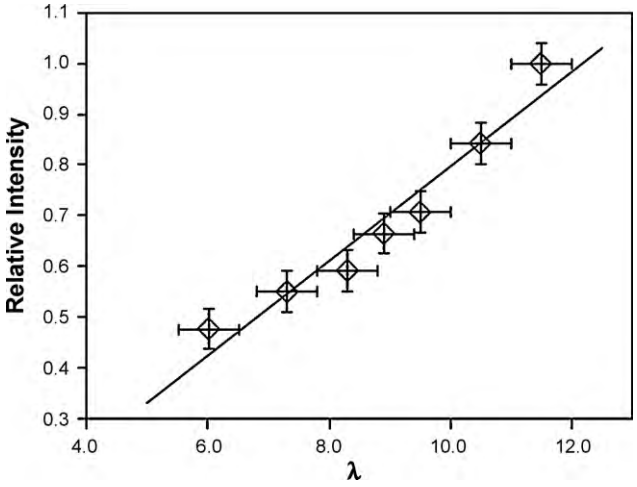

Fig. 3. Calibration curve relating the relative signal intensity of the ^{1}H MRI images to the λ values. This curve was determined using an unassembled PEM containing the MEA.

consist of at least three structurally-distinct phases and, when $\lambda \geq 5$, water begins to fill the pores in the membrane to form pathways as opposed to solvating the ionic groups. As λ becomes larger, water in the membrane is more bulk-like and as expected has longer ^{1}H $T_{2,obs}$ values.

The intensities of the eight echo images were used to calculate the ^{1}H $T_{2,obs}$ value for each PEM with known λ. The signal intensity of each echo image represents a fraction of the proton density, S_0 ($n = 0$ in Eq. (3)), and thus the individual images resulting from each echo could then be corrected to ^{1}H density-weighted images. Likewise, having determined the ^{1}H $T_{2,obs}$ value, the intensity of the image resulting from a sum of the eight individual $T_{2,obs}$-weighted images was corrected using the appropriate weighting function (i.e., $S(x,y) \propto \rho(x,y)\sum_n \exp(-nTE/T_{2,obs}(x,y))$) to determine the proton density image. Fig. 3 shows the correlation between the λ value and the corrected intensity of the corresponding ^{1}H MRI image. As expected, an approximately linear correlation between the proton density-weighted image intensities and λ was observed. Note that, when $\lambda < 6$, weak ^{1}H NMR signal prevented the extension of the calibration curve (Fig. 3). In these situations, mobility of the water molecules is likely to be more restricted, causing more rapid decay of the transverse ^{1}H NMR signal.

4.2. In situ water quantification

The reactant gas flow configuration (co- vs. counter-flow) of the cell affects the amount and the in-plane distribution of water in the PEM of an operating PEMFC. Because the counter-flow configuration allows a greater level of hydration and a more homogeneous distribution of water in the PEM than the co-flow configuration [49,50], the counter-flow configuration was used. Prior to operating the PEMFC, the anode flow field was filled with $H_2O(l)$ to fully hydrate the PEM. After purging $H_2O(l)$ from the anode flow field, ^{1}H MRI experiments were immediately performed. The in-plane ^{1}H MRI image acquired from a 0.5 mm slice containing the MEA of the PEMFC is shown in Fig. 4(a). As discussed in Section 3.1, the ROI in the ^{1}H MRI image of the fully hydrated PEM within the PEMFC is restricted to the MEA area (Fig. 4(b)), which is approximately 0.5 cm^2. The ionic conductivity in this area of the PEM has the greatest influence on cell performance; increased conductivity leads to higher currents and the production of more water at the cathode. The ^{1}H $T_{2,obs}$ value for the fully hydrated PEM in the PEMFC was determined to be 38 ± 3 ms. The ^{1}H $T_{2,obs}$ corrected intensity of

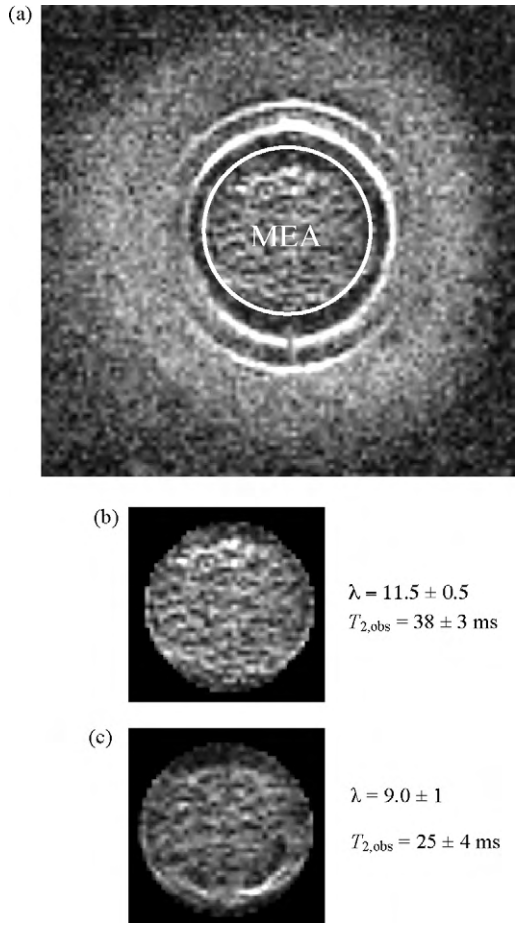

Fig. 4. (a) In-plane ^{1}H MRI image of the PEM in the PEMFC showing the MEA (i.e., the ROI). (b) ^{1}H MRI image of the ROI in the PEMFC after full hydration of the PEM. As described in the text, $\lambda = 11.5 \pm 0.5$ and $T_{2,obs} = 38 \pm 3$ ms. (c) ^{1}H MRI image of the ROI in the PEMFC operating at ~26.4 mW cm^{-2} (~20.0 mA, ~0.661 V) in the self-determined steady state. $\lambda = 9.0 \pm 1$ and $T_{2,obs} = 25 \pm 4$ ms. Image acquisition parameters for (a–c): SE, $TR = 1.0$ s, $TE = 3.2$ ms, FOV = 30 mm × 30 mm, pixel size = 234 μm × 234 μm, slice thickness = 0.5 mm, eight echoes per image, one average.

the ROI was taken as the intensity that can be assigned to the fully hydrated PEM (i.e., $\lambda = 11.5 \pm 0.5$) in the PEMFC. The ^{1}H $T_{2,obs}$ values and subsequently the ^{1}H $T_{2,obs}$ corrected signal intensity of the ROI of the PEM in the PEMFC under various operational conditions can be obtained using the aforementioned procedures. The corrected intensity for each operational state can be compared against that for $\lambda = 11.5 \pm 0.5$ to determine the relative signal intensity, and this ratio can then be used as the input to the calibration curve to derive the *in situ* λ value for this operational state.

As an example, the *in situ* λ value for the MEA operating at a power output of ~26.4 mW cm^{-2} (~20.0 mA, ~0.661 V) was determined after the cell reached a self-determined steady state of water in the MEA. Once the PEM is fully hydrated and operation of the cell starts, the water content in the PEM is self-adjusted as the electrochemical reaction proceeds. The dry reactant gases entering the flow channels draw water from the PEM and thus deplete water in the PEM. However, this is countered by water that is produced at the cathode, which can back diffuse from the cathode to the anode driven by the concentration gradient. Water is also transported from the anode to the cathode *via* electro-osmotic drag during the operation of the cell. All these processes are taking place simultaneously during the operation of the PEMFC, resulting in a steady state of water in the PEM. For the PEMFC operating at ~26.4 mW cm^{-2} (~20.0 mA, ~0.661 V) in the steady state, the ^{1}H $T_{2,obs}$ was 25 ± 4 ms yielding a relative intensity of 0.71 ± 0.09. Using the calibration plot

shown in Fig. 3 leads to a λ value of 9 ± 1. This value was obtained for the ROI (Fig. 4(c)), but could in principle be obtained for any specific region in the transverse-plane of the PEM.

5. Conclusions

These results demonstrate the *in situ* measurement of the transverse-plane λ within a Nafion® PEM between the operating catalyst layers of a PEMFC using ^{1}H MRI. Calibration curves that correlate λ with intensity of proton density weighted MRI images can be established under a variety of conditions. It is important that the history, pre-treatment, and the preparation of the MEA used to establish the calibration curve of relative ^{1}H NMR signal intensity versus λ matches those of the MEA in the operating fuel cell. Experiments are under way in these laboratories to use this technique to create *in situ* spatial and temporal maps of transverse-plane λ values within operating MEAs under a variety of operating conditions. The goal is to establish a fundamental scientific and practical understanding of water behavior in PEMFCs that can be applied to new PEMFC materials and designs, including PEMs that contain C–H bonds. Such a goal requires simultaneous measurement of water within all parts of the PEMFC. MRI currently provides *in situ* distribution of water within the flow field and the PEM of an operating PEMFC. Combinations of MRI, other experimental techniques reported in the literature, and modeling will lead to fundamental understandings of water within these systems.

Acknowledgements

The authors thank members of the solid-state NMR group at the University of Alberta for helpful discussion and comments. M.W. thanks the University of Alberta for funding. R.E.W. is a Canada Research Chair in Physical Chemistry and would like to thank the Government of Canada and the University of Alberta for financial support. This research has also been supported by the Natural Sciences and Engineering Research Council of Canada Discovery Grants to S.H.B. and R.E.W.

References

[1] G. Hoogers, Fuel Cell Technology Handbook, CRC Press LLC, Boca Raton, 2003.
[2] F. Barbir, PEM Fuel Cells: Theory and Practice, Elsevier Academic Press, San Diego, 2005.
[3] J. Larminie, A. Dicks, Fuel Cell Systems Explained, 2nd ed., John Wiley and Sons Ltd., Chichester, 2003.
[4] M. Eikerling, A.A. Kornyshev, A.R. Kucernak, Phys. Today 59 (2006) 38–44.
[5] S.D. Knights, K.M. Colbow, J. St-Pierre, D.P. Wilkinson, J. Power Sources 127 (2004) 127–134.
[6] J.R. Atkins, S.C. Savett, S.E. Creager, J. Power Sources 128 (2004) 201–207.
[7] M.A. Hickner, B.S. Pivovar, Fuel Cells 5 (2005) 213–229.
[8] M.V. Williams, H.R. Kunz, J.M. Fenton, J. Power Sources 135 (2004) 122–134.
[9] W.-M. Yan, C.-Y. Chen, S.-C. Mei, C.-Y. Soong, F. Chen, J. Power Sources 162 (2006) 1157–1164.
[10] T.A. Zawodzinski Jr., C. Derouin, S. Radzinski, R.J. Sherman, V.T. Smith, T.E. Springer, S. Gottesfeld, J. Electrochem. Soc. 140 (1993) 1041–1047.
[11] J.T. Hinatsu, M. Mizuhata, H. Takenaka, J. Electrochem. Soc. 141 (1994) 1493–1498.
[12] T.A. Zawodzinski Jr., T.E. Springer, J. Davey, R. Jestel, C. Lopez, J. Valerio, S. Gottesfeld, J. Electrochem. Soc. 140 (1993) 1981–1985.
[13] K.D. Kreuer, S.J. Paddison, E. Spohr, M. Schuster, Chem. Rev. 104 (2004) 4637–4678.
[14] K.A. Mauritz, R.B. Moore, Chem. Rev. 104 (2004) 4535–4585.
[15] A. Bazylak, Int. J. Hydrogen Energy 34 (2009) 3845–3857.
[16] J. St-Pierre, J. Electrochem. Soc. 154 (2007) B724–B731.
[17] F.N. Büchi, G.G. Scherer, J. Electrochem. Soc. 148 (2001) A183–188.
[18] M. Wakizoe, O.A. Velev, S. Srinivasan, Electrochim. Acta 40 (1995) 335–344.
[19] Y. Lee, B. Kim, Y. Kim, Int. J. Hydrogen Energy 34 (2009) 1999–2007.
[20] S. Slade, S.A. Campbell, T.R. Ralph, F.C. Walsh, J. Electrochem. Soc. 149 (2002) A1556–A1564.
[21] I.A. Schneider, H. Kuhn, A. Wokaun, G.G. Scherer, J. Electrochem. Soc. 152 (2005) A2092–A2103.
[22] I.A. Schneider, H. Kuhn, A. Wokaun, G.G. Scherer, J. Electrochem. Soc. 152 (2005) A2383–A2389.
[23] J. Stumper, C. Stone, J. Power Sources 176 (2008) 468–476.
[24] J. Stumper, M. Löhr, S. Hamada, J. Power Sources 143 (2005) 150–157.
[25] H. Görgün, M. Arcak, F. Barbir, J. Power Sources 157 (2006) 389–394.
[26] R.J. Bellows, M.Y. Lin, M. Arif, A.K. Thompson, D. Jacobson, J. Electrochem. Soc. 146 (1999) 1099–1103.
[27] R. Satija, D.L. Jacobson, M. Arif, S.A. Werner, J. Power Sources 129 (2004) 238–245.
[28] N. Pekula, K. Heller, P.A. Chuang, A. Turhan, M.M. Mench, J.S. Brenizer, K. Ünlü, Nucl. Instrum. Methods Phys. Res. Sect. A 542 (2005) 134–141.
[29] D. Kramer, J. Zhang, R. Shimoi, E. Lehmann, A. Wokaun, K. Shinohara, G.G. Scherer, Electrochim. Acta 50 (2005) 2603–2614.
[30] J. Zhang, D. Kramer, R. Shimoi, Y. Ono, E. Lehmann, A. Wokaun, K. Shinohara, G.G. Scherer, Electrochim. Acta 51 (2006) 2715–2727.
[31] M.A. Hickner, N.P. Siegel, K.S. Chen, D.N. McBrayer, D.S. Hussey, D.L. Jacobson, M. Arif, J. Electrochem. Soc. 153 (2006) A902–A908.
[32] I.A. Schneider, D. Kramer, A. Wokaun, G.G. Scherer, Electrochem. Commun. 7 (2005) 1393–1397.
[33] M.A. Hickner, N.P. Siegel, K.S. Chen, D.N. McBrayer, D.S. Hussey, D.L. Jacobson, M. Arif, J. Electrochem. Soc. 155 (2008) B427–B434.
[34] A.Z. Weber, M.A. Hickner, Electrochim. Acta 53 (2008) 7668–7674.
[35] C. Hartnig, I. Manke, R. Kuhn, S. Kleinau, J. Goebbels, J. Banhart, J. Power Sources 188 (2009) 468–474.
[36] A. Isopo, R. Albertini, J. Power Sources 184 (2008) 23–28.
[37] V.R. Albertini, B. Paci, F. Nobili, R. Marassi, Adv. Mater. 21 (2009) 578–583.
[38] H. Matic, A. Lundblad, G. Lindbergh, P. Jacobsson, Electrochem. Solid-State Lett. 8 (2005) A5–A7.
[39] Y.P. Patil, T.A.P. Seery, M.T. Shaw, R.S. Parnas, Ind. Eng. Chem. Res. 44 (2005) 6141–6147.
[40] L. Waller, J. Kim, Y. Shao-Horn, G. Barbastathis, Opt. Express 17 (2009) 14806–14816.
[41] Z. Dunbar, R.I. Masel, J. Power Sources 171 (2007) 678–687.
[42] K. Teranishi, S. Tsushima, S. Hirai, Therm. Sci. Eng. 10 (2002) 59–60.
[43] K. Teranishi, S. Tsushima, S. Hirai, Therm. Sci. Eng. 11 (2003) 31–32.
[44] K. Teranishi, S. Tsushima, S. Hirai, Therm. Sci. Eng. 12 (2004) 91–92.
[45] S. Tsushima, K. Teranishi, S. Hirai, Energy 30 (2004) 235–245.
[46] S. Tsushima, K. Teranishi, S. Hirai, Electrochem. Solid-State Lett. 7 (2004) A269–A272.
[47] S. Tsushima, K. Teranishi, K. Nishida, S. Hirai, Magn. Reson. Imaging 23 (2005) 255–258.
[48] K.R. Minard, V.V. Viswanathan, P.D. Majors, L.-Q. Wang, P.C. Rieke, J. Power Sources 161 (2006) 856–863.
[49] K.W. Feindel, S.H. Bergens, R.E. Wasylishen, ChemPhysChem 7 (2006) 67–75.
[50] K.W. Feindel, L.P.A. LaRocque, D. Starke, S.H. Bergens, R.E. Wasylishen, J. Am. Chem. Soc. 126 (2004) 11436–11437.
[51] Z. Zhang, J. Martin, J. Wu, H. Wang, K. Rpomishlow, B.J. Balcom, J. Magn. Reson. 193 (2008) 259–266.
[52] A. Hakenjos, H. Muener, U. Wittstadt, C. Hebling, J. Power Sources 131 (2004) 213–216.
[53] D.J. Ludlow, C.M. Calebrese, S.H. Yu, C.S. Dannehy, D.L. Jacobson, D.S. Hussey, M. Arif, M.K. Jensen, G.A. Eisman, J. Power Sources 162 (2006) 271–278.
[54] S. Tsushima, T. Nanjo, K. Nishida, S. Hirai, ECS Trans. 1 (2006) 199–205.
[55] Z.W. Dunbar, R.I. Masel, ECS Trans. 16 (2008) 1001–1008.
[56] K. Teranishi, S. Tsushima, S. Hirai, J. Electrochem. Soc. 153 (2006) A664–A672.
[57] T. Kotaka, S. Tsushima, S. Hirai, ECS Trans. 11 (2007) 445–450.
[58] T. Ikeda, T. Koido, S. Tsushima, S. Hirai, ECS Trans. 16 (2008) 1035–1040.
[59] S. Tsushima, S. Hirai, Fuel Cells 9 (2009) 506–517.
[60] S. Emid, J.H.N. Creyghton, Physica 128 (1985) 81–83.
[61] B.J. Balcom, in: P. Bluemler, B. Bluemich, R. Botto, E. Fukushima (Eds.), Spatially Resolved Magnetic Resonance: Methods, Materials, Medicine, Biology, Rheology, Geology, Ecology, Hardware, Wiley/VCH, Weinheim, Germany, 1998.
[62] M.D. Robson, P.D. Gatehouse, M. Bydder, G.M. Bydder, J. Comput. Assist. Tomogr. 27 (2003) 825–846.
[63] D.J. Tyler, M.D. Robson, R.M. Henkelman, I.R. Young, G.M. Bydder, J. Magn. Reson. Imaging 25 (2007) 279–289.
[64] E.M. Haache, R.W. Brown, M.R. Thompson, R. Venkatesan, Magnetic Resonance Imaging: Physical Principles and Sequence Design, John Wiley & Sons, New York, 1999.
[65] P.T. Callaghan, Principles of Nuclear Magnetic Resonance Microscopy, Oxford University Press, New York, 1991.
[66] B. Blümich, NMR Imaging of Materials, Oxford University Press, New York, 2000.
[67] R. Kimmich, NMR: Tomography, Diffusometry, Relaxometry, Springer-Verlag, Berlin, 1997.
[68] S. Stapf, S.-I. Han, in: S. Stapf, S.-I. Han (Eds.), NMR Imaging in Chemical Engineering, Wiley-VCH Verlag GmbH & Co. KGaA, Weinheim, 2006, pp. 1–45 (Chapter 1).
[69] J.A. Glasel, in: F. Franks (Ed.), Water: A Comprehensive Treatise, vol. 1 (Chapter 6), 1972.
[70] E.L. Hahn, Phys. Rev. 80 (1950) 580–582.
[71] T.C. Farrar, E.D. Becker, Pulse and Fourier Transform NMR—Introduction to Theory and Methods, Academic Press, New York, 1971.
[72] J. Kowalewski, L. Mäler, Nuclear Spin Relaxation in Liquids: Experiments, and Applications, Taylor and Francis, 2006.
[73] B. MacMillan, A.R. Short, R.L. Armstrong, Polymer 40 (1999) 2471–2480.
[74] D.X. Cao, S.H. Bergens, Electrochim. Acta 48 (2003) 4021–4031.

[75] K.W. Feindel, S.H. Bergens, R.E. Wasylishen, J. Am. Chem. Soc. 128 (2006) 14192–14199.
[76] K.W. Feindel, S.H. Bergens, R.E. Wasylishen, Phys. Chem. Chem. Phys. 9 (2007) 1850–1857.
[77] J.J. Fontanella, C.A. Edmondson, M.C. Wintersgill, Y. Wu, S.G. Greenbaum, Macromolecules 29 (1996) 4944–4951.
[78] R.S. Chen, P.E. Stallworth, S.G. Greenbaum, J.J. Fontanella, M.C. Wintersgill, Electrochim. Acta 40 (1995) 309–313.